Coulomb correlations in the honeycomb lattice: Role of translation symmetry

Ansgar Liebsch¹ and Wei Wu²

¹Peter Grünberg Institut, Forschungszentrum Jülich, 52425 Jülich, Germany ²Département de Physique and RQMP, Université de Sherbrooke, Sherbrooke, Québec J1K 2R1, Canada (Received 9 March 2013; published 20 May 2013)

The effect of Coulomb correlations in the half-filled Hubbard model of the honeycomb lattice is studied within the dynamical cluster approximation (DCA) combined with exact diagonalization (ED) and continuous-time quantum Monte Carlo (QMC), for unit cells consisting of six-site rings. The important difference between this approach and the previously employed cluster dynamical mean-field theory (CDMFT) is that DCA preserves the translation symmetry of the system, while CDMFT violates this symmetry. As the Dirac cones of the honeycomb lattice are the consequence of perfect long-range order, DCA yields semimetallic behavior at small on-site Coulomb interactions U, whereas CDMFT gives rise to a spurious excitation gap even for very small U. This basic difference between the two cluster approaches is found regardless of whether ED or QMC is used as the impurity solver. At larger values of U, the lack of translation symmetry becomes less important, so that the CDMFT reveals a Mott gap, in qualitative agreement with large-scale QMC calculations. In contrast, the semimetallic phase obtained in DCA persists even at U values where CDMFT and large-scale QMC consistently show Mott-insulating behavior.

DOI: 10.1103/PhysRevB.87.205127 PACS number(s): 71.10.-w, 73.22.-f

I. INTRODUCTION

The possible existence of a spin-liquid phase on the honeycomb lattice has recently attracted considerable attention. Meng et al. investigated the Hubbard model for this system at half filling, using large-scale quantum Monte Carlo (QMC) calculations for clusters containing up to 648 sites. Careful finite-size extrapolations indicated semimetallic behavior for on-site Coulomb interactions in the range $U \leq 3.5t$ (t is the nearest-neighbor hopping) and an antiferromagnetic insulator for $U \geqslant 4.3t$. The intermediate range $3.5t \leqslant U \leqslant 4.3t$ then corresponds to a Mott phase without long-range order, the hallmark of a spin liquid. These findings were, however, disputed by Sorella et al.² who performed similar QMC calculations for even larger clusters including up to 2592 sites. The new results showed a considerably reduced spin-liquid phase, confined at most to the narrow window $3.8t \le U \le$ 3.9t.

The effect of nonlocal Coulomb correlations on the honeycomb lattice was also studied within the cluster extension of dynamical mean-field theory³ (CDMFT). Wu et al.⁴ used continuous-time quantum Monte Carlo⁵ (CTQMC), whereas Liebsch⁶ employed a multiorbital-multisite extension^{7,8} of finite-temperature exact diagonalization⁹ (ED) as impurity solver. Despite the fact that in the ED CDMFT calculations it was possible to include only a relatively small bath (six bath levels per six-site ring unit cell), the cluster self-energy components were found to be in nearly quantitative agreement with the CTQMC CDMFT results. (For a detailed comparison see Fig. 25 of Ref. 10.) In particular, for $U \approx 5t$ both schemes revealed a Mott phase, with an excitation gap $\Delta \approx 0.6t$, in close agreement with the one found by Meng et al. With decreasing U, the CTQMC results at temperatures $T \ge 0.05t$ indicated the closing of the Mott gap near U = 3.8t, while the ED results at lower temperature T = 0.005t revealed a weak insulating contribution to the self-energy at the Dirac points at arbitrarily low U.⁶ For $U \leq 3t$ the small gap associated with this self-energy was, however, difficult to resolve in the

spectral distributions due to the temperature rounding of the gap edges.

Analogous ED CDMFT calculations (also for six bath levels per ring unit cell) were carried out by He and Lu¹¹ at a considerably lower effective temperature $(T=10^{-5}t)$. The excitation gap in this case was found to extend to $U \rightarrow 0$. On the basis of these results the authors concluded that the spin-liquid phase of the honeycomb lattice at half filling exists from U=0 up to the onset of the antiferromagnetic phase near U=4.5t.

Closely related to these works are two calculations based on the variational cluster approximation 12 (VCA) by Yu *et al.* 13 and Seki and Ohta. 14 In both cases, ED was used as impurity solver, with six bath levels as in Refs. 6 and 11. Whereas Yu *et al.* identified a spin-liquid phase in the range $U \approx 3t-4t$ and semimetallic behavior at smaller values of U, Seki and Ohta obtained a similar insulating contribution to the self-energy at the Dirac points as in Ref. 6 and concluded that the Mott gap persists down to arbitrarily small values of U.

Most recently, Hassan and Sénéchal¹⁵ performed ED calculations for the honeycomb lattice within VCA, CDMFT, and the cluster dynamical impurity approximation¹⁶ (CDIA). They argued that a bath consisting only of six levels per ring unit cell is insufficient and leads to the erroneous conclusion that the system is gapped for all nonzero values of the on-site Coulomb interaction U. In contrast, two- and four-site unit cells with two bath levels per site were shown to give rise to first-order transitions. In this context it is also important to recall the results of functional renormalization group (FRG) calculations¹⁷ for the honeycomb lattice which reveal a stable semimetallic phase below about $U \approx 3.8t$.

In view of these contradictory results it is evident that the possible existence and extent of the semimetallic phase of the honeycomb lattice are difficult to determine within present nonlocal many-body techniques. In particular, it is not clear which assumptions and approximations give rise to certain consequences: the size and shape of the correlated cluster,

the size and symmetry of the bath in ED, the accessible temperature range, the accuracy of spectral functions at very low energies, etc. Naturally, these uncertainties also affect the identification of the elusive spin-liquid phase.

The purpose of this work is to shed light on some of these issues by comparing new results derived within the dynamical cluster approximation ¹⁸ (DCA) with previous ones obtained within CDMFT. ^{4,6} As impurity solver we use finite-temperature ED as well as CTQMC. The nearly quantitative agreement between the ED and CTQMC self-energies, within DCA as well as CDMFT, demonstrates that the intrinsic limitations of these impurity solvers are not the cause of the discrepancies between the various results cited above.

Instead we show here that, for the six-site ring unit cell of the honeycomb lattice, it is of crucial importance to preserve the translational invariance of the system. In the case of this unit cell, deviations from bulk symmetry may readily open a gap at the Dirac points. Thus, the semimetallic and spinliquid phases can only be studied properly by using manybody methods that do not violate translation symmetry. This argument disqualifies CDMFT which is well known to yield a self-energy that is not translationally invariant. 19 The selfenergy components in this scheme account for correlations within the unit cell, but not between cells. We therefore believe that all CDMFT calculations performed until now for the ring unit cell of the honeycomb lattice should exhibit, at low U and low T, an excitation gap which is an artifact caused by the lack of translation symmetry of the self-energy. Although this gap is related to the presence of the local Coulomb interaction, it is not a true Mott gap but merely the consequence of the intrinsic limitation of the cluster approach. As a result, CDMFT and other schemes that do not preserve translation invariance are not suitable for the identification of a spin-liquid phase on the honeycomb lattice.

The comparison of the CDMFT self-energy with analogous results derived within DCA, for ED as well as CTQMC, underlines this point. In DCA, the self-energy is by construction translationally invariant, so that the electronic structure at low U is semimetallic, in agreement with the predictions based on large-scale QMC and FRG calculations. ^{1,2,17} The spurious tail of the excitation gap at small U and low T that is seen in CDMFT is absent in DCA.

As will be shown below, in the case of the honeycomb lattice, the DCA condition that ensures translation symmetry is too rigid for the description of correlations within the unit cell. As a result, the semimetallic phase is still stable near U=5t-6t where CDMFT and large-scale QMC calculations already find Mott-insulating behavior. Thus, CDMFT and DCA may be viewed as complementary cluster schemes: DCA is preferable at low U since it maintains the long-range order that is crucial for the Dirac cones, whereas CDMFT yields a more realistic description of short-range correlations in the Mott phase when the absence of translation symmetry plays a minor role.

We also note here that the gap tail obtained in CDMFT at small U is not related to the finite-size and symmetry properties of the bath used in ED. On the contrary, in the special case of the honeycomb lattice, a rather small bath containing only six levels is sufficient for the description of short-range correlations within the six-site unit cell. The reason

is that, because of the semimetallic properties of the system, the projection of the bath Green's function on a finite cluster is not affected by the usual low-energy disparities that arise in the case of correlated metals.

In this work, the focus is on the paramagnetic semimetallic and insulating phases of the Hubbard model of the honeycomb lattice at half filling. There is general consensus that the strong-coupling phase of this model is antiferromagnetic, with a critical Coulomb interaction of about $U_c \approx 4t-5t$. $^{1,4,11,13-15,17,20-23}$ Similar conclusions have been reached using lattice field theory methods for short-range as well as long-range Coulomb interactions. 24 As these results demonstrate, the chiral symmetry of the hexagonal lattice which gives rise to the linear dispersion of the energy bands in the vicinity of the Dirac cones is broken spontaneously once the interaction reaches a certain strength. In these models, a staggered field is introduced which serves as means to break the chiral symmetry, while periodic boundary conditions ensure semimetallic behavior at weak coupling.

The outline of this paper is as follows: In Sec. II we discuss the application of DCA and CDMFT to the honeycomb lattice and point out the key difference between the self-energies obtained within these schemes. Section III presents the main ingredients of the ED impurity solver for both DCA and CDMFT. Section IV provides the discussion of the results obtained within ED DCA, and the comparison with analogous CTQMC DCA results. The summary is presented in Sec. V.

II. DCA VERSUS CDMFT FOR THE HONEYCOMB LATTICE

To describe Coulomb correlations in the honeycomb lattice we consider the single-band Hubbard Hamiltonian

$$H = -t \sum_{\langle ij \rangle \sigma} (c_{i\sigma}^+ c_{j\sigma} + \text{H.c.}) + U \sum_i n_{i\uparrow} n_{i\downarrow}, \qquad (1)$$

where t is the nearest-neighbor hopping term and U the on-site Coulomb energy. Throughout this paper t=1 defines the energy scale. The noninteracting band dispersion is given by $\epsilon(\mathbf{k}) = \pm t |1 + e^{ik_x\sqrt{3}} + e^{i(k_x\sqrt{3} + k_y3)/2}|$. The nearest-neighbor spacing is assumed to be a=1. We choose a six-site ring unit cell with positions specified as $\mathbf{a}_1 = (0,0)$, $\mathbf{a}_2 = (0,1)$, $\mathbf{a}_3 = (\sqrt{3}/2,3/2)$, $\mathbf{a}_4 = (\sqrt{3},1)$, $\mathbf{a}_5 = (\sqrt{3},0)$, and $\mathbf{a}_6 = (\sqrt{3}/2,-1/2)$. The supercell lattice vectors are given by $\mathbf{A}_{1/2} = (3\sqrt{3}/2,\pm 3/2)$. For other unit cells, such as 2- and 4-site clusters, see Ref. 15.

Within CDMFT as well as DCA, the interacting lattice Green's function in the site basis is defined as

$$G_{ij}(i\omega_n) = \sum_{\mathbf{k}} \left[i\omega_n + \mu - h(\mathbf{k}) - \Sigma(i\omega_n) \right]_{ij}^{-1}, \quad (2)$$

where $\omega_n = (2n+1)\pi T$ are Matsubara frequencies and T is the temperature. At half filling, the chemical potential is $\mu = U/2$. The **k** sum extends over the reduced Brillouin zone, $h(\mathbf{k}) = -t(\mathbf{k})$, where $t(\mathbf{k})$ denotes the hopping matrix for the superlattice, and $\Sigma_{ij}(i\omega_n)$ represents the self-energy matrix in the site representation.

Within CDMFT, the elements of $t(\mathbf{k})$ within the unit cell are given by $t_{ij} = t$ for neighboring sites. In addition, hopping

between cells yields

$$t_{14} = t e^{-i\mathbf{k}\cdot\mathbf{A}_1}, \quad t_{25} = t e^{-i\mathbf{k}\cdot\mathbf{A}_2}, \quad t_{36} = t e^{-i\mathbf{k}\cdot\mathbf{A}_3}, \quad (3)$$

where $A_3 = A_2 - A_1$. The hopping matrix $t(\mathbf{k})$ is Hermitian, so that $t_{ji} = t_{ij}^*$. All other elements vanish.

To distinguish the hopping matrix elements within DCA, we denote them by $\bar{t}_{ij}(\mathbf{k})$. In the real-space version of DCA¹⁹ they are related to those within CDMFT via a phase factor:

$$\bar{t}_{ij} = t_{ij} e^{-i\mathbf{k}\cdot\mathbf{a}_{ij}}, \tag{4}$$

where $\mathbf{a}_{ij} = \mathbf{a}_i - \mathbf{a}_j$. This phase relation yields the following matrix elements:

$$\bar{t}_{12} = \bar{t}_{36} = \bar{t}_{54} = t e^{-i\mathbf{k} \cdot \mathbf{a}_{12}},
\bar{t}_{23} = \bar{t}_{41} = \bar{t}_{65} = t e^{-i\mathbf{k} \cdot \mathbf{a}_{23}},
\bar{t}_{34} = \bar{t}_{52} = \bar{t}_{16} = t e^{-i\mathbf{k} \cdot \mathbf{a}_{34}},$$
(5)

with analogous connections among the Hermitian elements. All other matrix elements vanish.

The cluster Hamiltonian in CDMFT has the hopping matrix elements $[\sum_{\mathbf{k}} t(\mathbf{k})]_{ij} = t_{ij}^{cl}$ where $t_{ij}^{cl} = t = 1$ for first neighbors and $t_{ij}^{cl} = 0$ otherwise. In contrast, in DCA we find $\bar{t}_{ij}^{cl} = \bar{t} = 0.8103$ for first and third neighbors and $\bar{t}_{ij}^{cl} = 0$ otherwise.

Within CDMFT as well as DCA, G_{ij} is a symmetric matrix, with site-independent diagonal components G_{ii} . Thus, the local density of states is sixfold degenerate. In the case of CDMFT, there are three independent off-diagonal elements: G_{12} , G_{13} , and G_{14} . Here, G_{11} , G_{13} are imaginary and G_{12} , G_{14} are real. Thus, the corresponding density of states components ρ_{11} and ρ_{13} are even functions of energy, while ρ_{12} and ρ_{14} are odd. In the case of DCA, translation symmetry is preserved, so that one has the additional condition $\rho_{12} = \rho_{14}$ and $G_{12} = G_{14}$ due to the equality of first- and third-neighbor hopping interactions \bar{t} .

Because of these symmetry properties, it is useful to express the lattice Green's function in the diagonal molecular-orbital basis whose elements $G_m(i\omega_n)$ $(m=1\cdots 6)$ are determined by

$$G_{1,2} = (G_{11} + 2G_{13}) \pm (G_{14} + 2G_{12}),$$

$$G_{3,4} = G_{5,6} = (G_{11} - G_{13}) \pm (G_{14} - G_{12}).$$
(6)

The unitary transformation \bar{T}_{im} linking the site and molecularorbital bases is defined in Eq. (6) of Ref. 6. Evidently, in CDMFT there are two independent complex functions, $G_1 = -G_2^*$ and $G_3 = -G_4^*$. In DCA, the elements $G_{m=3\cdots 6}$ are degenerate and imaginary. The on-site and intersite components of the lattice Green's function can be derived by inverting Eq. (6):

$$G_{11} = [(G_1 + G_2) + 2(G_3 + G_4)]/6,$$

$$G_{12} = [(G_1 - G_2) - (G_3 - G_4)]/6,$$

$$G_{13} = [(G_1 + G_2) - (G_3 + G_4)]/6,$$

$$G_{14} = [(G_1 - G_2) + 2(G_3 - G_4)]/6.$$
(7)

Figure 1 illustrates the uncorrelated density of states components in the diagonal molecular orbital basis, where $\rho_m(\omega) = -\frac{1}{\pi} \operatorname{Im} G_m(\omega)$. The total density of states is, of

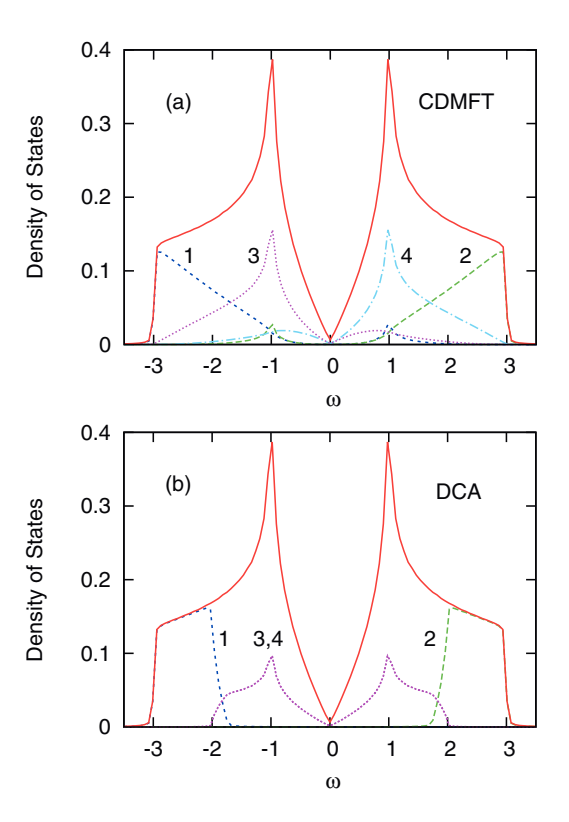


FIG. 1. (Color online) Density of states $\rho(\omega)$ (solid curves) of honeycomb lattice and cluster components $\rho_m(\omega)$ in diagonal molecular orbital basis (dashed curves) for (a) CDMFT and (b) DCA. For clarity, these components are divided by $n_c=6$. In CDMFT, all density components are nonsymmetric and orbitals 3 and 4 are doubly degenerate. In DCA, only ρ_1 and ρ_2 are nonsymmetric, while the degenerate components $\rho_{m=3\cdots 6}$ are symmetric. $\omega=0$ defines the Fermi energy for half filling.

course, the same within CDMFT and DCA, but its decomposition into molecular-orbital or intersite contributions differs for these two schemes. The four CDMFT densities shown in panel (a) are nonsymmetric and satisfy the relations $\rho_2(\omega) = \rho_1(-\omega)$ and $\rho_4(\omega) = \rho_3(-\omega)$. The corresponding DCA densities are plotted in panel (b). In this case, only $\rho_1(\omega) = \rho_2(-\omega)$ are nonsymmetric, whereas $\rho_3(\omega) = \rho_4(\omega)$ are symmetric.

Figure 2(a) shows the Brillouin zone of the honeycomb lattice together with the three times smaller reduced zone. Panel (b) illustrates the contributions to the density of states stemming from the outer \mathbf{k} regions KMK'M' and the inner regions $\Gamma M'K'$. These two contributions overlap slightly since the point K' does not lie halfway between Γ and M. Thus, the low-energy part of the density of states (denoted as K) extends up to $|\omega| \leq 2$, while the high-energy part (denoted as Γ) corresponds to the window $1.75 \le |\omega| \le 3$. The comparison with Fig. 1(b) shows that the diagonal elements of the DCA density of states correspond to the distributions indicated in Fig. 2(b). Thus, $\rho_{1,2}(\omega)$ account for the energy bands in the inner regions $\Gamma M' K'$ and $\rho_{3,4}(\omega)$ for those in the outer regions KMK'M' of the original Brillouin zone. The momentum regions shown in Fig. 2(a) therefore specify the appropriate tiling of the Brillouin zone within the DCA.

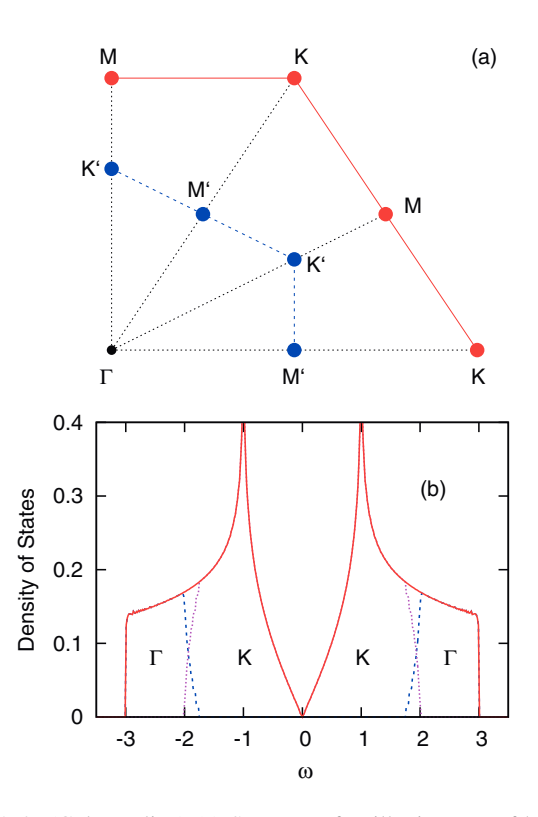


FIG. 2. (Color online) (a) Segment of Brillouin zone of honeycomb lattice (solid red lines). The reduced zone (dashed blue lines) is obtained by folding the Dirac points K onto Γ and the M points onto M'. (b) Decomposition of density of states into low-energy contribution (denoted as K) corresponding to outer regions KMK'M' and high-energy contribution (denoted as Γ) corresponding to inner regions $\Gamma M'K'$ of large Brillouin zone.

The self-energy matrices in CDMFT and DCA satisfy the same symmetry properties as the lattice Green's functions so that they can be diagonalized in the same manner. These diagonal elements will be denoted as $\Sigma_m(i\omega_n)$. In the site basis the components Σ_{11} and Σ_{13} are imaginary, whereas Σ_{12} and Σ_{14} are real. As translation symmetry is not obeyed in CDMFT, Σ_{12} and Σ_{14} differ, while in DCA they coincide

We point out that although the hopping matrix elements $t(\mathbf{k})$ in CDMFT and DCA differ only by a unitary transformation as indicated in Eq. (4), the same does not hold for the respective self-energy matrices. As discussed below, the preservation of translation invariance in DCA and its absence in CDMFT give rise to fundamentally different physical solutions which severely affect the phase boundaries. Thus, the DCA and CDMFT self-energy matrices are not simply related via a unitary transformation.

Severe differences of this kind between DCA and CDMFT do not arise in the case of the Hubbard model for the square lattice, where the cluster Hamiltonians maintain the same symmetry. The only difference is that the hopping interaction between neighbors is changed from t=1 in CDMFT to $\bar{t}=1.273$ in DCA. As a result, these cluster schemes lead to a less dramatic reorganization of spectral weight among the cluster components than in the case of the honeycomb lattice.

III. EXACT DIAGONALIZATION

To avoid double counting of Coulomb interactions in the quantum impurity calculation, the self-energy must be removed from the six-site cluster in which correlations are treated explicitly. This removal yields the bath Green's function matrix

$$G_0(i\omega_n) = [G(i\omega_n)^{-1} + \Sigma(i\omega_n)]^{-1}.$$
 (8)

Within the ED approach, this bath Green's function of the infinite lattice is projected onto the corresponding function of a supercluster consisting of $n_c = 6$ correlated sites within the unit cell plus a bath consisting of n_b discrete levels. Here, we choose $n_b = 6$, so that the total number of levels of the supercluster is $n_s = n_c + n_b = 12$. Within the diagonal molecular-orbital basis, this projection implies

$$G_{0,m}(i\omega_n) \approx G_{0,m}^{cl}(i\omega_n)$$

$$= \left(i\omega_n + \mu - \epsilon_m - \sum_{k=7}^{12} \frac{|V_{mk}|^2}{i\omega_n - \epsilon_k}\right)^{-1}, \quad (9)$$

where $\epsilon_{m=1\cdots 6}$ denotes impurity levels and $\epsilon_{k=7\cdots 12}$ bath levels. The bath levels are defined relative to the chemical potential. We assume that the molecular orbitals couple to independent baths so that the hybridization matrix elements are also diagonal in this representation: $V_{mk} = \delta_{m+6,k} V_k$. Figure 3(a) illustrates the impurity and bath levels in the diagonal molecular orbital basis. Panel (b) shows the equivalent representation when the impurity orbitals are transformed to the original site basis. The bath remains unchanged and the hopping terms in this basis are given by $V_{ik} = \sum_m \bar{T}_{im} V_{mk}$. This picture differs from the one in which also the bath is treated within the site basis (see below).

To determine the bath levels ϵ_k and hopping terms V_{mk} we minimize the difference

Diff_m =
$$\sum_{n=0}^{M} W_n^N |G_{0,m}(i\omega_n) - G_{0,m}^{cl}(i\omega_n)|^2$$
, (10)

where $M \approx 2^{10}$ is the total number of Matsubara points and the weight function $W_n^N = 1/\omega_n^N$ is introduced to give more weight to the low-frequency region. We usually take N=1 or N=2. Note also that both Green's functions in the above expression approach $1/i\omega_n$ for large ω_n . Thus the difference defined in Eq. (10) automatically focuses on the low-energy region. This is not the case when the differences of the inverse Green's functions are minimized instead. The reason is that the hybridization functions corresponding to $G_{0,m}$ and $G_{0,m}^{cl}$ are not normalized to the same asymptotic amplitudes. To start the iterative procedure, we use bath parameters obtained for the uncorrelated system, or from a converged solution for nearby Coulomb energies. The resulting ϵ_k and V_{mk} are usually very stable against variations of initial conditions.

In the CDMFT calculations discussed in Ref. 6, not only the bath levels ϵ_k and hopping elements V_k were used as parameters in the fit of $G_{0,m}(i\omega_n)$, but also the impurity levels ϵ_m . Since the expression Eq. (9) ensures the correct asymptotic behavior, the variation of ϵ_m yields slightly better accuracy of the fit at the lower Matsubara points. For each diagonal component $G_{0,m}$ three fit parameters are then available. As

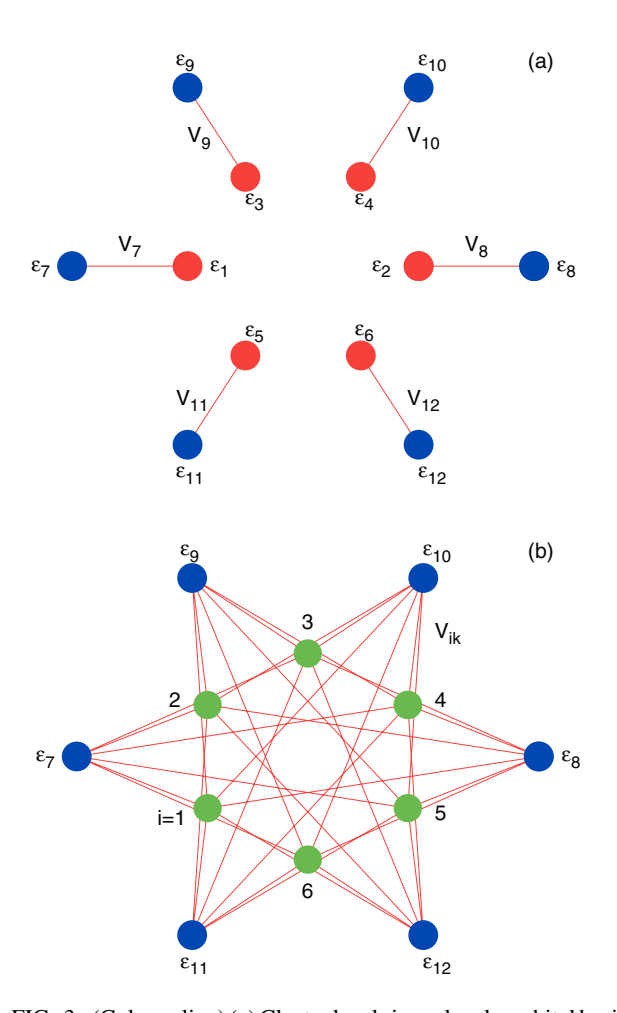


FIG. 3. (Color online) (a) Cluster levels in molecular orbital basis. There are six independent terms connecting orbital levels $\epsilon_{m=1\cdots 6}$ (red dots) and bath levels $\epsilon_{k=7\cdots 12}$ (blue dots) via hopping integrals $V_{k=7\cdots 12}$. In CDMFT (for fixed impurity levels) one has $\epsilon_{1,2} = \pm 2t$, $\epsilon_{3,4} =$ $\epsilon_{5,6} = \pm t$, and $\epsilon_7 = -\epsilon_8$, $\epsilon_9 = \epsilon_{11} = -\epsilon_{10} = -\epsilon_{12}$, $V_7 = V_8$, $V_9 =$ $V_{10} = V_{11} = V_{12}$. Thus there are four independent bath parameters. In DCA, $\epsilon_{1,2} = \mp 3\bar{t}$, $\epsilon_{3\cdots 6} = \epsilon_{9\cdots 12} = 0$; i.e., there are only three independent fit parameters. (b) Cluster levels in site basis $i = 1 \cdots 6$ (green dots) connected to molecular orbital bath levels $\epsilon_{k=7\cdots 12}$ (blue dots) via hopping integrals V_{ik} . For clarity, the hopping interactions between impurity sites are not shown. Representations (a) and (b) are equivalent since they are connected via the unitary transformation \bar{T} between impurity sites $i = 1 \cdots 6$ and orbitals $m = 1 \cdots 6$. The bath molecular orbital levels in (b) are the same as in (a). Thus, although the cluster sites have identical levels at zero energy, the bath levels maintain the orbital symmetry.

there are only two independent complex functions $G_{0,m}$, the total number of parameters to fit the bath is six. As shown in Fig. 24 of Ref. 10 for U=4 and T=0.01, this procedure yields a surprisingly good reproduction of the lattice bath Green's function via the cluster Anderson Green's function, in spite of the fact that we use only one bath level per impurity orbital. The reason for this good fit is the semimetallic nature of the honeycomb lattice, giving rise to a vanishing density of states at the Fermi level. In contrast, in ordinary correlated metals and the triangular or square lattice Hubbard models, the density of states of the infinite lattice is finite, so that a successful fit to a cluster Green's function usually requires at

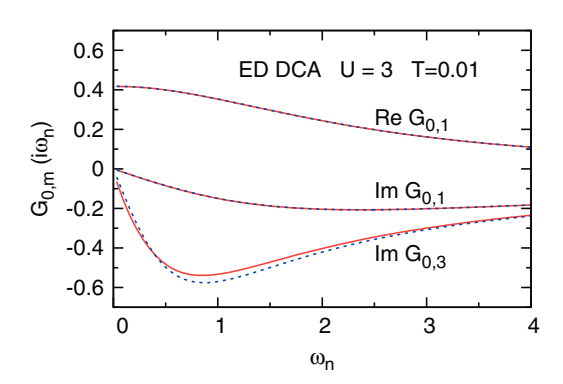


FIG. 4. (Color online) Comparison of lattice bath Green's function $G_{0,m}(i\omega_n)$ (solid red curves) and cluster Green's function (dashed blue curves) for U=3 and T=0.01. As the density of states for m=3 is symmetric in DCA [see Fig. 1(b)], $G_{0,3}$ is purely imaginary, while $G_{0,1}$ is complex. Thus, the latter function is fitted with two parameters, whereas $G_{0,3}$ involves only one fit parameter. The solid and dashed curves for $G_{0,1}$ are indistinguishable.

least two bath levels per orbital and restriction to not very low temperatures (typically $T \ge 0.01$).

In the DCA calculations presented below, we fix the impurity levels ϵ_m at their nominal cluster values. Thus, $\epsilon_{1,2}=\mp 3\bar{t}$ and $\epsilon_{3,4}=0$. The latter value reflects the fact that the DCA density of states components $\rho_{3,4}(\omega)$ are even functions of energy. Thus, the fit of $G_{0,m=1,2}$ involves two parameters (the bath level $\epsilon_7=-\epsilon_8$ and the hopping element $V_7=V_8$), while $G_{0,m=3,4}$ includes only the hopping element $V_9=V_{10}$ as fit parameter.

Figure 4 illustrates the quality of the fit of G_0 within ED DCA for U=3 and T=0.01. The parameters used in these fits are $\epsilon_1=-3\bar{t}=-2.4309, \epsilon_7=-1.85694, V_7=0.26270$ for m=1 and $\epsilon_3=\epsilon_9=0$, $V_9=0.86701$ for m=3. As pointed out above in the case of CDMFT, the excellent representation of the lattice Green's function via the cluster Green's function using only one bath level per impurity orbital is related to the vanishing density of states at the Fermi level.

The diagonalization of the supercluster Hamiltonian is conveniently carried out in the site basis. At low temperatures only a few excited states need to be included in the evaluation of the cluster Green's function $G_{ij}^{cl}(i\omega_n)$. The diagonalization can then be performed very efficiently by making use of the Arnoldi algorithm. Details concerning this procedure are provided in Refs. 7,8 and 10. Since the cluster Green's function obeys the same symmetry properties as the lattice Green's function, it is diagonal in the molecular-orbital basis. These elements will be denoted as $G_m^{cl}(i\omega_n)$. The diagonal cluster self-energy components are then given by an expression analogous to Eq. (8):

$$\Sigma_{m}^{cl}(i\omega_{n}) = 1/G_{0\,m}^{cl}(i\omega_{n}) - 1/G_{m}^{cl}(i\omega_{n}). \tag{11}$$

The key physical assumption in DMFT is now that this cluster self-energy provides an accurate representation of the lattice self-energy. Thus,

$$\Sigma_m(i\omega_n) \approx \Sigma_m^{cl}(i\omega_n).$$
 (12)

In the next iteration, these self-energy components are used as input in the lattice Green's function Eq. (2). In the diagonal molecular-orbital basis the DCA lattice Green's function is

given by

$$G_m(i\omega_n) = \sum_{\mathbf{k}} [i\omega_n + \mu - \bar{T}^{-1}\bar{h}(\mathbf{k})\bar{T} - \Sigma(i\omega_n)]_{mm}^{-1}. \quad (13)$$

We note here that, at real energies, the cluster quantities G_m^{cl} , $G_{0,m}^{cl}$, and Σ_m^{cl} have discrete spectra, while the corresponding lattice spectra associated with the quantities G_m , $G_{0,m}$, and Σ_m are continuous.

We close this section by pointing out that we believe the projection of the bath Green's function within the diagonal molecular-orbital basis discussed above to be more general and more flexible than analogous projections within the nondiagonal site basis. As mentioned above, within CDMFT there are two independent complex functions $G_{0,m}$ (with nonsymmetric spectral distributions) that are fitted each with one bath level ϵ_k and one hopping term V_k (assuming the impurity level ϵ_m to be fixed). Thus, there are altogether four fit parameters. This should be compared to only one fit parameter if the site basis is used instead. For symmetry reasons all bath levels then are zero so that only the site independent impurity bath hopping element remains as a single-fit parameter. Introducing a hopping interaction among bath levels as was done in Ref. 11 increases the number of fit parameters from one to two. Actually, since the bath can always be represented in a diagonal form, hopping among bath levels is implicitly included in the diagonal molecular orbital picture with four fit parameters. Analogous considerations hold for DCA. Nevertheless, as will be shown in the next section, these slightly different implementations of ED all yield consistent answers concerning the variation of the excitation gap as a function of Coulomb energy.

IV. RESULTS AND DISCUSSION

Figure 5 shows the comparison of the excitation gaps obtained for various cluster methods and impurity solvers. Near $U \approx 5$, all calculations (except DCA, see below) predict a Mott phase with a gap $\Delta \approx 0.5$ –0.9. At $U \leqslant 4$, the CDMFT

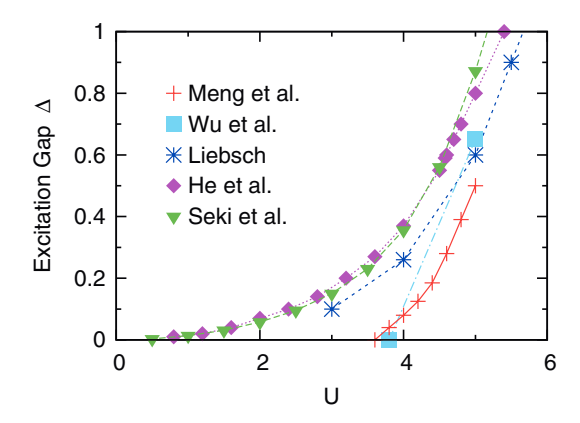


FIG. 5. (Color online) Comparison of excitation gaps as functions of Coulomb interaction derived using several cluster methods and impurity solvers for paramagnetic phase of honeycomb lattice. Meng *et al.*: large-scale QMC (Ref. 1), Wu *et al.*: CTQMC CDMFT (Ref. 4), Liebsch: ED CDMFT (Ref. 6), He *et al.*: ED CDMFT (Ref. 11), Seki *et al.*: ED VCA (Ref. 14). In contrast, both ED and CTQMC DCA yield semimetallic behavior with $\Delta = 0$ for $U \le 6$ (see text).

and VCA results that do not preserve translation symmetry exhibit a gap tail that persists down to $U \to 0$. The differences between these results are partly caused by the different temperatures used in these studies. In particular, the gap closing near U=3.8 obtained within CDMFT by Wu $et~al.^4$ seems to be related to the rather high temperature, T=0.05, employed in the CTQMC calculation. Since the CTQMC self-energy agrees well with the ED results, CTQMC CDMFT presumably would also yield a gap at lower T. Also, the ED calculations in Ref. 6 were carried out at T=0.005, while those in Refs. 11 and 14 essentially correspond to the $T\to 0$ limit.

In striking contrast to CDMFT, the translation invariance of DCA ensures the existence of a semimetallic phase at low values of U. On the other hand, the condition $\Sigma_{12} = \Sigma_{14}$ cannot generally be correct for the short-range correlations within the unit cell. Thus, at Coulomb energies, where local Mott physics dominates and long-range translational invariance becomes less important, DCA should be less appropriate than CDMFT. Indeed, both ED and CTQMC DCA results suggest that the semimetallic phase with $\Delta=0$ extends to U>6, i.e., beyond the critical Coulomb energy $U_c\approx 3.9$ –4.3 of the antiferromagnetic phase. 1.2

This is illustrated in Fig. 6, which shows the interacting density of states obtained in ED and CTQMC DCA for several Coulomb energies. The ED spectra were obtained by making

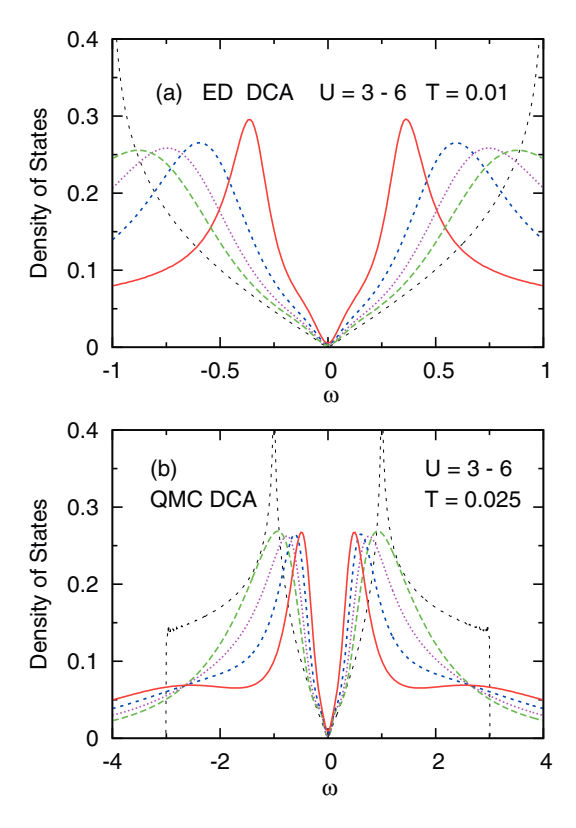


FIG. 6. (Color online) Density of states $A_{11}(\omega) = -\frac{1}{\pi} \text{Im } G_{11}(\omega)$ of honeycomb lattice for several Coulomb energies. Red solid curves: U=6, dashed curves: U=3-5. (a) ED DCA (T=0.01). (b) CTQMC DCA (T=0.025). For illustrative purpose, only the low-energy range of the ED spectra is shown. The dotted curve denotes the bare density of states.

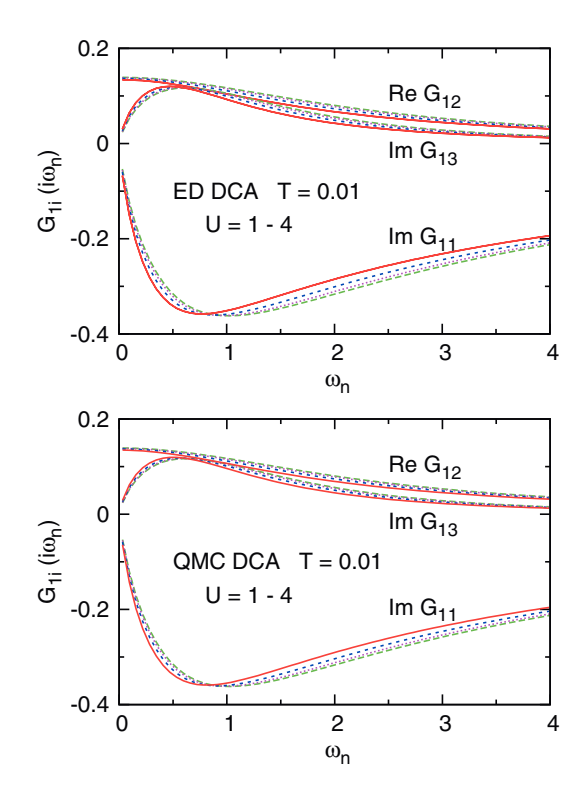


FIG. 7. (Color online) Green's function components $G_{1i}(i\omega_n)$ (i=1,2,3) of honeycomb lattice as functions of Matsubara frequency calculated within (a) ED DCA and (b) CTQMC DCA at T=0.01. Solid red curves: U=4; dashed curves: U=1-3.

use of the extrapolation routine RATINT, ²⁵ while the CTQMC spectra were derived via the maximum entropy method. ²⁶ For details concerning the CTQMC calculations, see Ref. 4. The main effect of Coulomb interactions is seen to be the usual band narrowing and effective mass enhancement, as found in weakly correlated systems. In contrast, the corresponding ED and CTQMC CDMFT spectra for U=5 reveal a large Mott gap of about $\Delta=0.6$ (see Fig. 5). ^{4,6}

The persistence of semimetallic behavior at large U within DCA is related to the fact that the enforcement of translation symmetry is achieved at the expense of equating first- and third-neighbor interactions in the cluster Hamiltonian. The self-energy in the site basis then satisfies the condition $\Sigma_{12} = \Sigma_{14}$, whereas in CDMFT Σ_{14} is noticeably smaller than Σ_{12} .

The good correspondence between the DCA spectra obtained within ED and CTQMC is a consequence of the nearly quantitative agreement of the lattice Green's functions $G_{1i}(i\omega_n)$ which are shown in Fig. 7. As pointed out in the preceding section, for symmetry reasons G_{11} and G_{13} are imaginary, while $G_{12}=G_{14}$ are real. Both impurity solvers yield $\operatorname{Im} G_{11}(i\omega_n) \to 0$ in the limit $\omega_n \to 0$, implying that the local density of states, $\rho(\omega) = -\frac{1}{\pi} \operatorname{Im} G_{11}(\omega)$ vanishes at $\omega=0$. Also, both schemes indicate that with increasing values of U the initial slope of $\operatorname{Im} G_{11}$ and $\operatorname{Im} G_{13}$ increases. Thus, the Dirac cones become steeper and spectral weight is shifted towards the Fermi level.

The results obtained within DCA differ in two qualitative aspects from those derived previously in CDMFT. As shown in Fig. 8, the components G_{12} and G_{14} in CDMFT do not

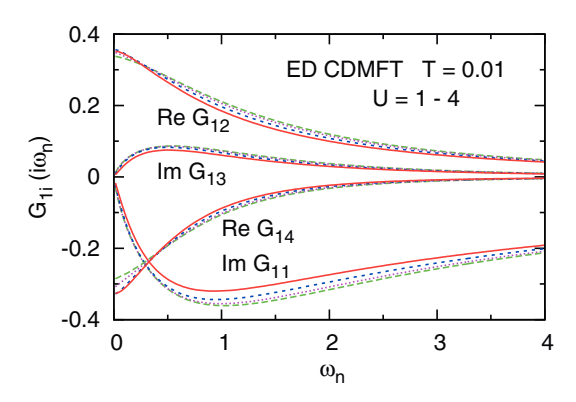


FIG. 8. (Color online) Green's function components $G_{1i}(i\omega_n)$ (i=1,2,4) of honeycomb lattice as functions of Matsubara frequency calculated within ED CDMFT. Solid red curves: U=4; dashed curves: U=1-3.

coincide. Moreover, the initial slopes of $\operatorname{Im} G_{11}$ and $\operatorname{Im} G_{13}$ become smaller with increasing U rather than larger as within DCA. In Ref. 6 it was demonstrated that for $U \geqslant 4$ a Mott gap opens in the density of states, in approximate agreement with the large-scale QMC calculations by Meng $et\ al.^1$ At smaller values of U, a tiny gap or pseudogap was also found (see below), which is however difficult to resolve within ED at finite T. As the opening of a gap in the density of states implies a reduction of $|\operatorname{Im} G_{11}(i\omega_n)|$ at small values of ω_n , the results shown in Figs. 7 and 8 underline the fundamental difference between DCA and CDMFT for the honeycomb lattice: Whereas DCA yields a weakly correlated semimetal, CDMFT gives rise to insulating behavior even at small U.

To illustrate the effect of Coulomb correlations in more detail, we show in Fig. 9 the self-energy components in the site basis for several values of U. The corresponding results obtained within CTQMC DCA are depicted in Fig. 10. There is good overall correspondence between these two impurity solvers, except for slightly different magnitudes of the off-diagonal components. We note, however, that Re Σ_{12} and Im Σ_{13} are approximately one and two orders of magnitude smaller than Im Σ_{11} , respectively. As can be seen in Fig. 7, these differences have only a minor effect on the variation of the Green's function components with increasing Coulomb energy.

The crucial question in the case of the honeycomb lattice is how Coulomb correlations influence the energy bands in the vicinity of the Dirac points. The self-energy at these points can be shown to have the simple form⁶

$$\Sigma(K, i\omega_n) \approx i\omega_n a + \frac{b^2}{i\omega_n (1-a)}, \quad \omega_n \to 0,$$
 (14)

where the coefficients are given by

$$a = \operatorname{Im}[\Sigma_{11}(i\omega_n) - \Sigma_{13}(i\omega_n)]/\omega_n, \tag{15}$$

$$b = \text{Re}[\Sigma_{12}(i\omega_n) - \Sigma_{14}(i\omega_n)] \tag{16}$$

in the limit $\omega_n \to 0$. Thus, $\Sigma(K, i\omega_n)$ is imaginary as expected for particle-hole symmetry near the Dirac points. Moreover, this self-energy consists of metallic $(\sim i\omega_n)$ and insulating $(\sim 1/i\omega_n)$ contributions, where the latter term is a direct consequence of the fact that $\Sigma_{12} \neq \Sigma_{14}$. The presence of this

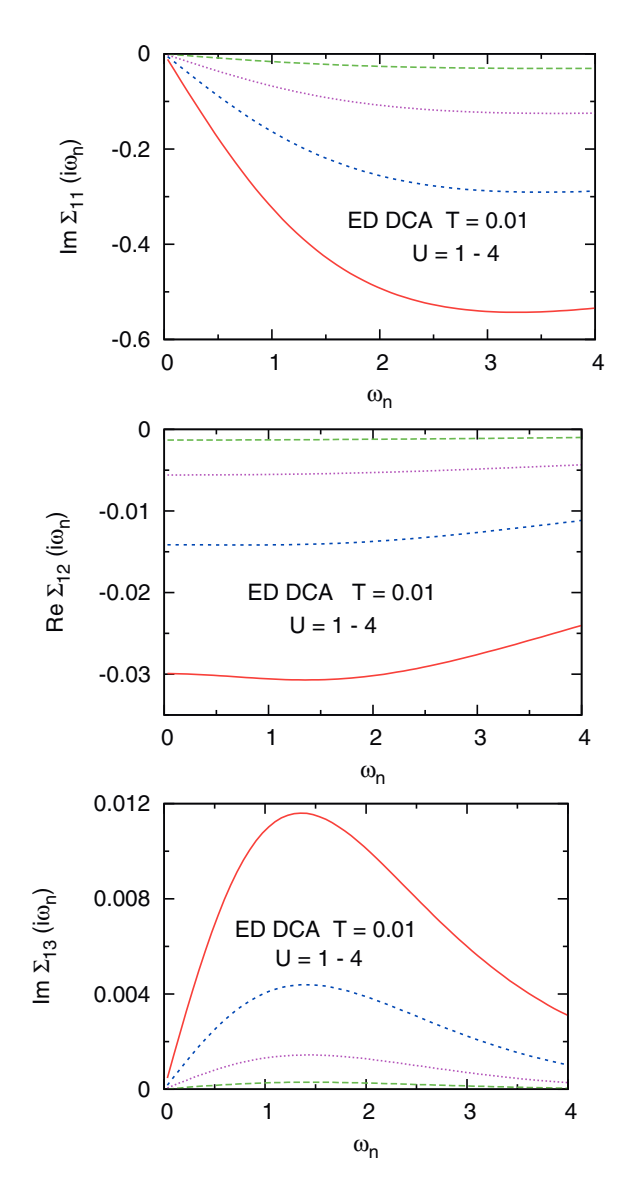


FIG. 9. (Color online) Self-energy components $\Sigma_{1i}(i\omega_n)$ (i=1,2,3) of honeycomb lattice as functions of Matsubara frequency calculated within ED DCA for U=1–4 at T=0.01.

term implies $\operatorname{Re} \Sigma(K,\omega) \approx b^2/[\omega(1-a)]$ at real ω . In the low-temperature limit, this expression yields an excitation gap of magnitude $\Delta \approx 2\sqrt{|c|}$, where $c=b^2/(1-a)$. A similar insulating contribution to the self-energy was recently found in Ref. 14. Presumably, this insulating term is also present in the ED calculations reported in Refs. 11 and 13. At finite T, the gap is smoothened out so that it becomes difficult to determine its boundaries. In contrast, as discussed in Sec. II, DCA preserves the bulk symmetry, so that $\Sigma_{12} = \Sigma_{14}$ and $\Delta = 0$. Thus, the DCA self-energy at the Dirac points is purely metallic, where the increasing magnitude of the coefficient a implies increasing quasiparticle broadening and shift of spectral weight towards the Fermi level as U increases. From the initial slope of $\operatorname{Im} \Sigma_{11}$ at U=4 we obtain an effective mass enhancement of about $m^*/m \approx 1.3$.

The above discussion demonstrates that the presence or absence of the insulating contribution to $\Sigma(K,i\omega_n)$ is not caused by the impurity solver used in the CDMFT or DCA

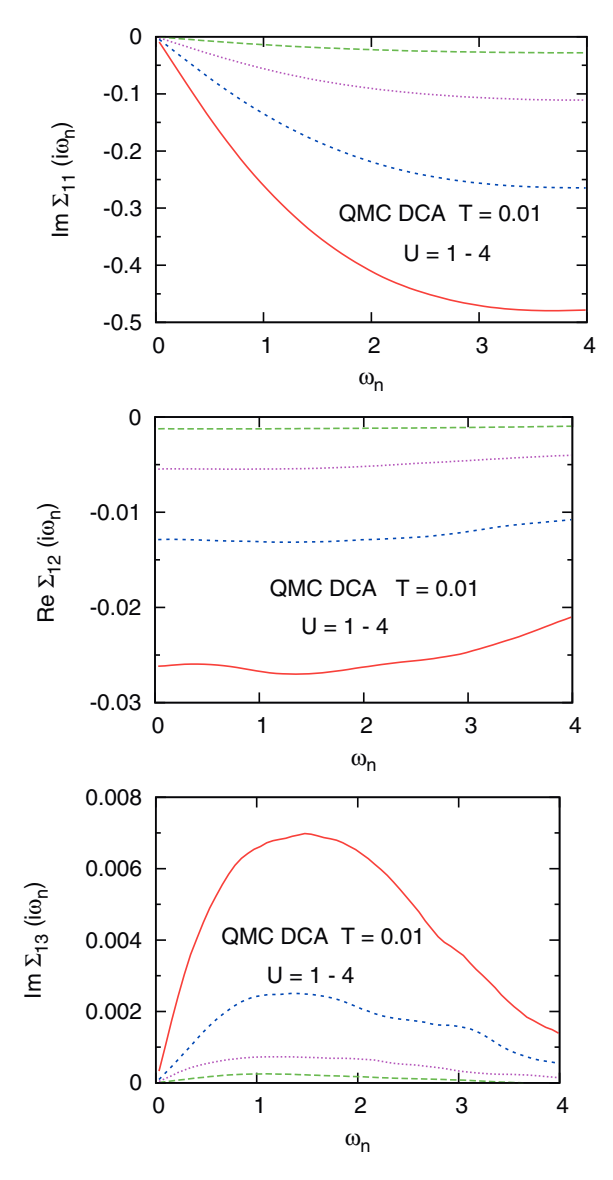


FIG. 10. (Color online) Self-energy components $\Sigma_{1i}(i\omega_n)$ (i=1,2,3) of honeycomb lattice as functions of Matsubara frequency calculated within CTQMC DCA for U=1–4 at T=0.01.

calculations. In fact, the good agreement between ED and CTQMC, for both CDMFT and DCA, suggests that in the case of the honeycomb lattice one bath level per impurity orbital is sufficient for an accurate fit of the bath Green's function. The reason is that, because of the semimetallic nature of the honeycomb lattice, the projection of the bath Green's function of the infinite lattice onto a finite-cluster Anderson Green's function is not plagued by the low-energy-low-temperature discrepancies that usually occur in the case of correlated metals. In these systems at least two bath levels per impurity orbital are typically required and very low temperatures must be avoided. ¹⁰

The focus of this section is on the paramagnetic phase of the honeycomb lattice derived within two impurity solvers and two cluster extensions of DMFT. We close this discussion by commenting briefly on the antiferromagnetic phases obtained at strong coupling. Within CTQMC CDMFT we had shown previously⁴ that $U_c \approx 3.7t$, in approximate agreement with other schemes. [1,11,13–15,17] Analogous CTQMC DCA

calculations yield a slightly smaller value, $U_c \approx 3.3t$. The difference is presumably related to the fact pointed out above, namely, that the enforcement of translation symmetry within DCA implies the condition $\Sigma_{12} = \Sigma_{14}$, which accounts properly for interactions between unit cells, but which is surely unrealistic within the ring unit cell, in particular, at large U, where short-range correlations dominate. Thus, in this range, CDMFT should provide a more adequate description of the cluster self-energy.

V. SUMMARY

The role of Coulomb correlations in the Hubbard model for the honeycomb lattice has been studied within finitetemperature exact diagonalization and continuous-time quantum Monte Carlo combined with the dynamical cluster approximation. The unique feature of DCA is that it preserves the translation invariance so that the system at small values of U is semi-metallic. In contrast, CDMFT violates translation symmetry which, in the case of ring unit cells, implies the opening of an excitation gap at arbitrarily small U, regardless of the impurity solver. This gap is therefore an artifact caused by the lack of long-range crystal symmetry and does not correspond to a true Mott gap. At larger values of U, however, many-body interactions are dominated by short-range correlations and translation symmetry ceases to be important. DCA then becomes less accurate since it overemphasizes semimetallic behavior. Thus, for $U \approx 5$, CDMFT is preferable and reveals a Mott gap in qualitative agreement with large-scale QMC calculations.

In the case of the ring unit cell of the honeycomb lattice, DCA and CDMFT may therefore be viewed as complementary cluster approaches. As DCA preserves translation symmetry, it is more appropriate in the semimetallic phase at small U where long-range order is a prerequisite for the description of

the weakly correlated Dirac cones. The condition $\Sigma_{12} = \Sigma_{14}$ which guaranties this symmetry, however, is unrealistic at larger U, when short-range correlations within the unit cell begin to dominate. Thus, in the region of the Mott phase, CDMFT is more suitable. As a result of these inherent limitations of both cluster schemes, the critical Coulomb interaction defining the precise boundary between these phases is at present difficult to determine within either CDMFT or DCA. We emphasize that this difficulty is not related to the finite size or symmetry of the bath used in ED. On the contrary, within CDMFT as well as DCA, the ED self-energies agree remarkably well with the corresponding CTQMC results.

It is interesting to inquire why the remarkable difference between CDMFT and DCA for the honeycomb lattice discussed in this paper does not also manifest itself in other systems, such as the Hubbard models for square and triangular lattices. In these cases, long-range order is mainly responsible for the logarithmic divergence of the Van Hove singularities of the density of states. Thus, any lack of perfect translation symmetry would give rise to a rounding of this peak, an effect that would be difficult to distinguish from broadening induced by finite temperature and quasiparticle damping. In contrast, any rounding of Dirac cones induces the opening of a gap. In this regard, the Dirac cones of the honeycomb lattice correspond to a rather peculiar special situation that does not arise in most cases which have been studied previously within CDMFT and DCA at finite temperatures.

ACKNOWLEDGMENTS

The ED DCA calculations were carried out on the Jülich Juropa machine. W.W. acknowledges support from the Natural Sciences and Engineering Research Council of Canada. A.L. would like to thank Z.-Y. Lu and K. Seki for sending their data shown in Fig. 5.

¹Z. Y. Meng, T. C. Lang, S. Wessel, F. F. Assaad, and A. Muramatsu, Nature (London) **464**, 847 (2010).

²S. Sorella, Y. Otsuka, and S. Yunoki, Sci. Rep. 2, 992 (2012).

³G. Kotliar, S. Y. Savrasov, G. Palsson, and G. Biroli, Phys. Rev. Lett. **87**, 186401 (2001).

⁴W. Wu, Y.-H. Chen, H.-Sh. Tao, N.-H. Tong, and W.-M. Liu, Phys. Rev. B **82**, 245102 (2010); see also W. Wu, S. Rachel, W.-M. Liu, and K. Le Hur, *ibid*. **85**, 205102 (2012).

⁵A. N. Rubtsov, V. V. Savkin, and A. I. Lichtenstein, Phys. Rev. B **72**, 035122 (2005).

⁶A. Liebsch, Phys. Rev. B **83**, 035113 (2011).

⁷C. A. Perroni, H. Ishida, and A. Liebsch, Phys. Rev. B **75**, 045125 (2007).

⁸A. Liebsch and N.-H. Tong, Phys. Rev. B **80**, 165126 (2009).

⁹M. Caffarel and W. Krauth, Phys. Rev. Lett. **72**, 1545 (1994).

¹⁰ A. Liebsch and H. Ishida, J. Phys.: Condensed Matter 24, 053201 (2012)

¹¹R.-Q. He and Z.-Y. Lu, Phys. Rev. B **86**, 045105 (2012).

¹²M. Potthoff, Eur. Phys. J. B **32**, 429 (2003); M. Potthoff, M. Aichhorn, and C. Dahnken, Phys. Rev. Lett. **91**, 206402 (2003).

¹³S.-L. Yu, X.-C. Xie, and J.-X. Li, Phys. Rev. Lett. **107**, 010401 (2011).

¹⁴K. Seki and Y. Ohta, arXiv:1209.2101.

¹⁵S. R. Hassan and D. Sénéchal, Phys. Rev. Lett. **110**, 096402 (2013).

¹⁶M. Potthoff, in *Theoretical Methods for Strongly Correlated Systems*, Springer Series in Solid-State Sciences, Vol. 171, edited by A. Avella and F. Mancini (Springer, New York, 2012), Chap. 9.

¹⁷C. Honerkamp, Phys. Rev. Lett. **100**, 146404 (2008); S. Raghu, X.-L. Qi, C. Honerkamp, and S.-C. Zhang, *ibid*. **100**, 156401 (2008).

¹⁸M. H. Hettler, A. N. Tahvildar-Zadeh, M. Jarrell, T. Pruschke, and H. R. Krishnamurthy, Phys. Rev. B 58, R7475 (1998); Th. A. Maier, M. Jarrell, T. Pruschke, and M. H. Hettler, Rev. Mod. Phys. 77, 1027 (2005)

¹⁹G. Biroli, O. Parcolett, and G. Kotliar, Phys. Rev. B **69**, 205108 (2004); G. Biroli and G. Kotliar, *ibid*. **65**, 155112 (2002).

²⁰S. Sorella and E. Tosatti, Europhys. Lett. **19**, 699 (1992).

²¹L. M. Martello, M. Dzierzawa, L. Siffert, and D. Baeriswyl, Z. Phys. B **103**, 335 (1997).

²²T. Paiva, R. T. Scalettar, W. Zheng, R. R. P. Singh, and J. Oitmaa, Phys. Rev. B **72**, 085123 (2005).

- S. Hands, and C. Strouthos, *ibid.* **84**, 075123 (2011); and references herein.
- ²⁵Numerical Recipes in Fortran 77 (Cambridge University Press, 1986–1992), p. 106.
- ²⁶M. Jarrell and J. E. Gubernatis, Phys. Rep. **269**, 133 (1996).

²³F. F. Assaad and I. F. Herbut, arXiv:1304.6340.

²⁴See, e.g., M. V. Ulybyshev, P. V. Buividovich, M. I. Katsnelson and M. I. Polikarpov, arXiv:1304.3660; J. E. Drut and T. A. Lähde, arXiv:1304.1711; Y. Araki and G. W. Semenoff, Phys. Rev. B 86, 121402(R) (2012); D. Soriano and J. Fernández-Rossier, *ibid.* 85, 195433 (2012); J. González, *ibid.* 85, 085420 (2012); W. Armour,